Non-spherical particle trajectory modelling for ice crystal conditions

Author, co-author (Do NOT enter this information. It will be pulled from participant tab in MyTechZone)

Affiliation (Do NOT enter this information. It will be pulled from participant tab in MyTechZone)

Abstract

Aircraft icing is a significant issue for aviation safety. In this paper, recent developments for calculating the trajectory of non-spherical particles are used to determine the trajectory and impingement of ice crystals in aircraft icing scenarios. Two models are used, each formulated from direct numerical simulations, to give the drag, lift and torque correlations for various shaped particles. Previously, within the range of Reynolds number permitted in this study, it was only possible to model the trajectory and full rotational progression of cylindrical particles. The work presented in this paper allows for analysis of a wider range of ice shapes that are commonly seen in icing conditions, capturing the dynamics and behaviours specific to ice crystals. Previous limitations relate to the in ability to account for particle rotation and the dependency of force correlations on the measure of particle sphericity – which are now overcome. The method also provides an opportunity for new analysis – the creation of catch bounds for mixed clouds of particles. The above models are applied to two geometries and compared with drag only cases for spheres and non-spherical particles as parameterized by sphericity.

The analysis shows that taking the worst- and best-case scenarios provide a range of values for the catch, which can help to understand better the extent over which particles impinge. Hence a catch-limit for a mixed cloud of particles of different shaped particles and different sized particles may be easily gained. The methods are also able to capture rotations and trajectories in three dimensions. Incorporating new methods for modelling the trajectory, rotation and orientation of non-spherical particles into the modelling of aircraft icing opens new avenues for industrial analysis. In turn this may aide several areas of aircraft design related to engine design and flight instrumentation system design as well as informing the aircraft certification process.

Introduction

From 1997, aircraft icing was on the United States National Transportation Safety Board (NTSB) 'Most Wanted List' for safety improvements [1]. Whilst significant improvements have been made throughout the industry in recent years, aircraft icing continues to be a contributory factor in accidents and incidents. Given the hazard posed by ice crystals, aviation regulations were expanded by the Federal Aviation Administration to include ice crystals and account for the threat to air safety. In particular, two chapters on the airworthiness standards for transport planes and aircraft engines (14 CFR 25 and 14 CFR 33, respectively [2]) include: Appendix C – atmospheric icing conditions describing key icing conditions; and Appendix D – mixed phase and ice crystal icing envelope (deep convective clouds) to describe ice crystal icing conditions. Whilst it is vital for aircraft manufacturers to comply with these regulations, presently there are still difficulties in demonstrating compliance, particularly with ice particles – the concern of this paper.

With the continued increase in world-wide air travel, aircraft are routinely operating in areas of the world where severe icing conditions are more prevalent. Ice crystal events occur mainly at high altitudes, at cold temperatures and in the neighbourhood of convective cloud systems [3]. Aviation generally has a very good safety record considering the number of flights undertaken every day. However, there is still a need to keep improving this record as the frequency and volume of air travel increases, especially given the catastrophic consequences of severe icing events. (For example, in 2009, aircraft icing contributed to the loss of an Air France Airbus A330 aircraft with all 228 passengers and crew. This was, at least in part, attributed to mis-reading of the airspeed system because of ice crystal impacts and ice formation [4].)

In working towards reducing the number of incidents and accidents it is required that capability in modelling techniques is improved in combination with ground testing (icing wind tunnels) and flight testing [5]. There have been two issues which have meant that such work has not previously been performed [6]. The first issue was that knowledge of the detailed physics of the phenomena was missing. This has been addressed to some extent by numerous research programmes around the world (e.g. those conducted by NASA Lewis Research Centre, Official National d'Etudes et de Recherches Aérospatiales (ONERA), CIRA, the HAIC programme and its associated partners). Much of this work has focussed on the detection of ice crystal clouds and the physics of ice accretion. This research forms an important basis for the development of numerical models of ice crystal trajectories and impact behaviours. Whilst these research programmes have had a significant impact on the field of aircraft icing, industrial application requires rapid analysis methods. Hence, the second issue is the integration of the methods into industrial codes. The aeronautical industry requires problems to be solved in a practical time-scale, which often requires simplifying assumptions to be made. This in-turn must be balanced to meet acceptable thresholds of accuracy and realism for use in showing compliance with current flight safety requirements and the necessary certification. Such assumptions can only be made with thorough understanding of the problem and detailed knowledge of the limitations.

The ability to predict the behaviour of ice crystals is essential for the certification and improved design of anti-icing systems. The low cost of computational modelling and large amount of data and scenarios that can be analysed makes such modelling a convenient option given the recent technological and computational developments [7]. However, performing large scale simulations for whole aircraft geometries can be very time consuming. Ice crystals are more complex to model compared to droplets in as much as the shape, size and thus trajectory of ice particles can vary greatly. Notably, ice crystals may grow up to 2mm in size and form into a wide range of shapes [8]. The complex ice shapes and increased particle mass thus affect their trajectory and response in the airflow. Particularly, for droplets a spherical or near spherical assumption may be made regarding the particle shape, such that only the drag force needs to be considered. By contrast, it is common for ice particles to take on disc-like or cylindrical shapes, introducing

asymmetry and the need to consider the particle's orientation, rotational evolution, torques and lift forces.

Given the complexities, many approaches could be taken. In order to capture the intricacies of the real world physics to potential methods are direct numerical simulation (DNS) [9] or coupled computational fluid simulations (CFS) (e.g. [10]). These can vary in complexity and may be used to fully model the coupled flow-particle systems including the detailed internal and external pressure responses that affect an evolving particle trajectory, the present turbulence and temperature effects. Particularly, they require that the Navier-Stokes equations are solved numerically, and that the spatial and temporal scales of the turbulence are resolved. However, such methods are time consuming, requiring large computational power and effort to produce highly accurate and realistic results that are of little relevance for industrial analysis since only small-time spans can be feasibly modelled [11]. This is an issue when performing ice crystal and impingement modelling for industrial purposes since models for large segments of aircraft, or in some cases whole aircraft, are required. As a result, these coupled, highly physical methods increase the computational intensity required, hence such models are not widely implementable or usable in industry.

An alternative however is to use these advanced methods or experimental data to produce approximate methods for the force and torque coefficients. These derived correlations may be used to approximate the resultant behaviour of a particle in a flow. A survey of these methods was carried out in [12]. The authors covered a range of methods that may be used to define and quantify the particle shape and how the force and torque correlations may be calculated. This approach is reasonable in aircraft icing scenarios since the concentration of droplets is small such that they have negligible aerodynamic effect on the freestream flow, and thus particle trajectories may be modelled as an independent, uncoupled system.

Of note is the particle's sphericity - a parameter used to define the shape of a particle in relation to how it deviates from that of an ideal sphere [13]. Parameterising particle's in this way helps to simplify the analysis of different shapes as particles may simply be described by two parameters, by its sphericity and size (diameter). Though, there is a limitation - vastly different shaped particles, for which very different responses to the air flow may be expected, may each have the same parameter values, Figure 1. This is partly due to sphericity not accounting for the particle orientation. One method that is widely used is that of [14] [15] in which two forms of sphericity are defined in lengthwise (in the direction of the flow) and crosswise (perpendicular to the flow) directions, adding an orientation to the effective sphericity, however this can prove complicated to calculate in practice.

In this paper, drag, lift and torque correlations are used to determine the trajectory and impingement of ice particles in aircraft icing scenarios for various shaped particles. Thus far there are few papers that use such methods to address the scenario of aircraft icing. In this paper the correlations from [7] and [16] are both used. These are both formulated from DNS of the particle progression. In [7] force and torque correlations are given for four specific particle shapes, Figure 1. These correlations allow for the modelling of several precisely defined particle shapes: an ellipsoid of aspect ratio 5/2, an ellipsoid of aspect ratio 5/4, a disc of aspect ratio 5/1 and a cylinder of aspect ratio 5/1. The limitations of these correlations however lie in the lack of flexibility of particle shape and that are only verified for $0 < Re_p \leq 300$, where Re_p is the particle Reynolds number, see Appendix A for further details.

In [16] force and torque correlations are prolate ellipsoids of aspect ratio $w \in [1, 32]$, Figure 2. The limitations of these correlations are that they have only been verified for $0 < Re_p \leq 240$, where Re_p is the particle Reynolds number. Furthermore, both sets of correlations have been derived for a particle angle $\alpha \in [0,90]$. This however is not a significant limitation due to the symmetry of the particles.

The advantage of these correlations over others is their direct dependence on the particle orientation, that each distinct shape is treated differently, and that each force (drag and lift) and torque has its own correlation (this differs from usual methods where lift is gained from the drag coefficient and the pitching torque is derived from the forces). Furthermore, since they have been derived from DNS their formulation helps to overcome limitations with gaining experimental data.

In section 2, the details of the method used to model the particle trajectory are given, specifying how the particle orientation is tracked and calculated. In section 3, the computational method are briefly detailed. The analysis and comparison of methods are then presented in section 4. Beginning with a simple symmetrical case and working through to a more complex case, the impingement and catch of each particle type is calculated showing how each deviate from a spherical particle trajectory – given a range of particle. To conclude this paper, the method and results are discussed, with the limitations and possible directions for future work highlighted.
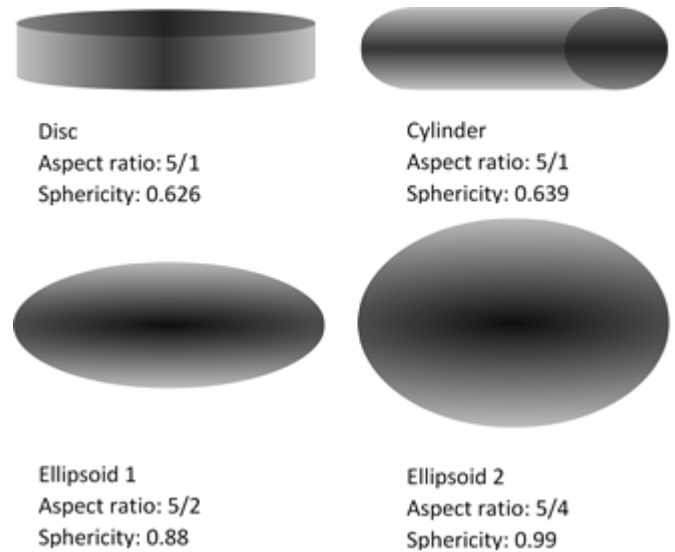

Figure 1: Examples (not to scale) of four non-spherical particles for which correlations are formulated in [7].
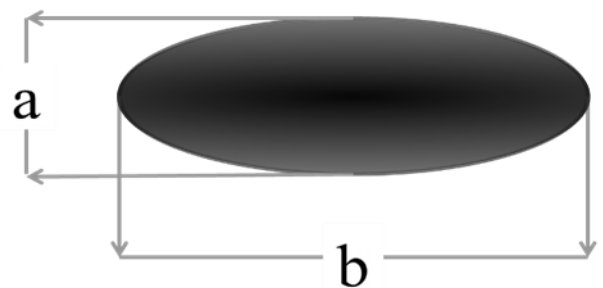

Figure 2: Aspect ratio $w = \frac{b}{a}$, $b > a$ of elliptical particles for which correlations are formulated in [16].

A note on OpenFOAM v1812

The method was implemented in the latest release from OpenCFD Ltd, OpenFOAM version 1812. This is an open source computational fluid dynamics software that possesses a wide range of features and may be used to solve a range of complex fluid problems including chemical reactions to turbulence and heat transfer. Coupled and non-coupled systems of fluid particle models can be modelled – with several solvers available for calculating aerodynamic solutions and Lagrangian particle motions. The computational method used in this work is detailed later.

Modelling the motion of non-spherical particles

Equations of motion

For the rotational motion of a non-spherical body, two Cartesian co-ordinate systems are required, one relating to the particle's orientation (x_B, y_B, z_B) and the other to a global frame (x_G, y_G, z_G) in which the fluid flow is solved, Figure 3. As a result, the parameters that govern the fluid flow and particle trajectory may be considered in relation to either co-ordinate system (denoted by a superscript G in the global frame and superscript B for the particle's frame – no superscript implies either frame may be considered).

The mapping between the particle's orientation and global co-ordinate system is defined using unit Quarternions. Whilst it is also intuitive to use Euler angles, it is well known that Euler angles suffer from singularities when sequential rotations occur, causing the angles to change by up to 2π [17]. As a result, unit Quarternions are used instead to track the rotation of the particles.
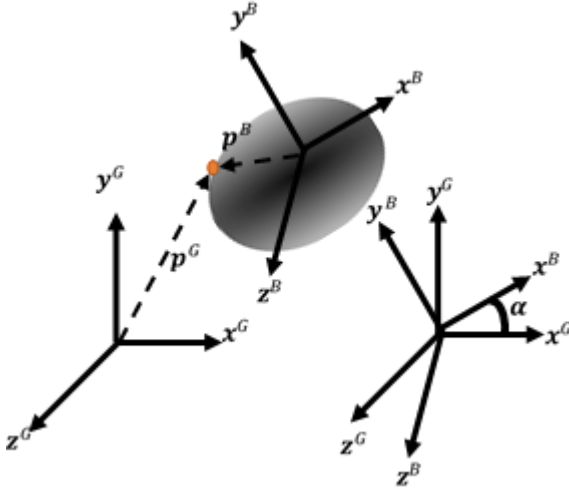

Figure 3: The global frame of reference and body frame of reference can be rotated between using Quarternions. α denotes the angle between the global x-axis and body x-axis.

Rotations are expressed by generalised co-ordinates defined by $q = [q_0, \boldsymbol{q}]$, where q_0 is the scalar part, and $\boldsymbol{q} = [q_1, q_2, q_3]$ is the vector part. Hence, there is a total of 4 unknowns. The unit Quarternion q is expressed by the angle of rotation, β and vector around which the rotation takes place $\hat{\boldsymbol{n}}$:

$$q = \left[\cos\left(\frac{\beta}{2}\right), \sin\left(\frac{\beta}{2}\right)\hat{\boldsymbol{n}}\right], \|q\| = \sqrt{q_0^2 + q_1^2 + q_2^2 + q_3^2} = 1,$$

Rotating between the global x-axis, x^G, and the particle's x-axis, x^B, q is calculated as follows:

1. Define: $\tilde{q}_0 = \|x^G\| \|x^B\| + x^G \circ x^B = \|x^G\| \|x^B\|(1 + \cos(\alpha)).$

2. Define: $\tilde{\boldsymbol{q}} = x^G \times x^B = \|x^G\| \|x^B\| \sin(\alpha) \hat{\boldsymbol{n}},$ where $\hat{\boldsymbol{n}}$ is the unit normal vector orthogonal to both x^G and x^B.

3. Normalise $\tilde{q}$ such that $q = \frac{\tilde{q}}{\|\tilde{q}\|}$ where:

$$\|\tilde{q}\| = \|x^G\|\|x^B\|\sqrt{1 + 2\cos(\alpha) + \cos^2(\alpha) + \sin^2(\alpha)\left(\hat{n}_1^2 + \hat{n}_2^2 + \hat{n}_3^2\right)}$$
$$= \|x^G\|\|x^B\|\sqrt{2 + 2\cos(\alpha)},$$

Thus, for $i = 1,2,3$

$$q_0 = \frac{\tilde{q}_0}{\|\tilde{q}\|} = \frac{1 + \cos(\alpha)}{\sqrt{2 + \cos(\alpha)}} = \sqrt{\frac{1 + \cos(\alpha)}{2}} = \cos\left(\frac{\alpha}{2}\right),$$

$$q_i = \frac{\tilde{q}_i}{\|\tilde{q}\|} = \frac{\sin(\alpha)}{\sqrt{2 + \cos(\alpha)}}\hat{n}_i = \sqrt{\frac{1 - \cos(\alpha)}{2}}\hat{n}_i = \sin\left(\frac{\alpha}{2}\right)\hat{n}_i.$$

Using unit Quarternions, a rotation matrix may be constructed to rotate between co-ordinate frames without scaling the rotated vector (an issue that occurs with generalised Quarternions [18]):

$$\boldsymbol{R(q)} = \begin{bmatrix} 1 - 2q_2^2 - 2q_3^2 & 2q_1q_2 + 2q_0q_3 & 2q_1q_3 - 2q_0q_2 \\ 2q_1q_2 - 2q_0q_3 & 1 - 2q_1^2 - 2q_3^2 & 2q_2q_3 + 2q_0q_1 \\ 2q_1q_3 + 2q_0q_2 & 2q_2q_3 - 2q_0q_1 & 1 - 2q_1^2 - 2q_2^2 \end{bmatrix} \quad (1)$$

$$x^B = \boldsymbol{R(q)}\, x^G, \quad x^G = \boldsymbol{R}^T(\boldsymbol{q})\, x^B .$$

Using the two co-ordinate frames, the trajectory and evolution of a non-spherical particle's position and orientation can be calculated. The motion of the particle is calculated in the frame of the fluid – the global frame – whilst the rotation of the particle is calculated in body co-ordinates. For a body's translational position and velocity, with centre of mass at $\boldsymbol{x}_p^G(t) := \left[x_p^G(t), y_p^G(t), z_p^G(t)\right]^T$, the set of equations is:

$$\frac{d\boldsymbol{x}_p^G(t)}{dt} := \boldsymbol{U}_p^G(t), \quad (2)$$

$$m_p \frac{d\boldsymbol{U}_p^G(t)}{dt} := \boldsymbol{F}_L^G(t) + \boldsymbol{F}_D^G(t). \quad (3)$$

where $\boldsymbol{U}_p^G(t)$ is the particle's velocity, m_p is the particle's mass, $\boldsymbol{F}_L^G(t)$ is the lift force acting on the particle and $\boldsymbol{F}_D^G(t)$ is the drag force. The equations of motion that describe the rotation of non-spherical particles and the change in their orientation are:

$$\frac{d\boldsymbol{\varphi}_p^B(t)}{dt} := \boldsymbol{\omega}_p^B(t), \quad (4)$$

$$\boldsymbol{I}_p^B \frac{d\boldsymbol{\omega}_p^B(t)}{dt} + \boldsymbol{\omega}_p^B(t) \times \left(\boldsymbol{I}_p^B \boldsymbol{\omega}_p^B(t)\right) = \boldsymbol{T}_P^B(t) + \boldsymbol{T}_R^B(t), \quad (5)$$

$$\boldsymbol{I}_p^B := \begin{bmatrix} I_x^B & 0 & 0 \\ 0 & I_y^B & 0 \\ 0 & 0 & I_z^B \end{bmatrix}. \quad (6)$$

where $\boldsymbol{\omega}_p^B(t)$ is the angular momentum of the particle, $\boldsymbol{I}_p^B$ is the matrix of inertial terms for the regularly shaped, axis-symmetric particles; $\boldsymbol{T}_P^B(t)$ is the pitching torque of the particle and $\boldsymbol{T}_R^B(t)$ is the rotational torque for the particle. The equations (2)-(6) together give a 10 ODE system for this fluid-particle system that is solved simultaneously.

Particle velocity

Assuming only a drag and lift force acting on the particle, the particle velocity is given by:

$$\frac{d\boldsymbol{u}_p}{dt} = \frac{\boldsymbol{F}_L + \boldsymbol{F}_D}{m_p}, \quad (7)$$

$$m_p = \rho_p \frac{4}{3}\pi\left(\frac{d_{eq}}{2}\right)^3, \quad (8)$$

where d_{eq} is the diameter of the volume equivalent sphere as found by:

$$\text{Particle volume} = \frac{4}{3}\pi\left(\frac{d_{eq}}{2}\right)^3.$$

The fluid exerts two types of force on the particle: drag force in the direction of the flow and a lift force acting perpendicular to the flow. These are calculated using correlations, listed in Appendix A. The magnitude of these correlations may be dependent on the shape, orientation and particle Reynolds number Re_p defined:

$$Re_p = \frac{\rho_p \, \mu \, |\tilde{u}^G|}{d_{eq}}. \tag{9}$$

where $\tilde{u}^G = u_f^G - u_p^G$ is the relative velocity. The drag force acts in the direction of the relative fluid flow $\tilde{u}^G$, such that:

$$F_D^G = \frac{1}{2} C_D(Re_p, \alpha) A_p \rho_f |\tilde{u}^G| \tilde{u}^G, \tag{10}$$

Here $A_p = {}^\pi/_4 \, d_p^2$ is the area of the volume equivalent sphere. Hence the contribution to particle velocity is given by:

$$\begin{aligned}
\frac{du_D^G}{dt} &= \frac{\frac{1}{2} C_D(Re_p, \alpha) \frac{\pi}{4} d_{eq}^2 \, \rho_f |\tilde{u}^G| \tilde{u}^G}{\rho_p \frac{4}{24} \pi \, d_{eq}^3} \\
&= \frac{3 \, C_D(Re_p, \alpha) \, \mu_f \, Re_p}{4 \, \rho_p \, d_{eq}^2} \tilde{u}^G.
\end{aligned} \tag{11}$$

The angle of incidence between the particle and the fluid flow is denoted α with $\sin(\alpha) = x^G \times \tilde{u}^G / |\tilde{u}^G|$. Explicit formulas for each correlation are provided in Appendix A.

Next, the lift force F_L^G is to be calculated. Acting perpendicular to the relative fluid flow, the size of the force F_L is:

$$F_L^B = \frac{1}{2} C_L(Re_p, \alpha) A_p \rho |\tilde{u}|^2 L^B, \tag{12}$$

$$F_L^G = R_q^T F_L^B.$$

The vector L^B is a unit vector which determines the direction of the lift force. Notably, the contribution in the y^B and z^B directions are such due to the symmetry of the body about the x^B-axis (for discs the formulae for the x and y directions need to be swapped since disc particles are symmetrical about the y-axis. The expressions are analogous) [19].

$$L_x^B = \frac{|x^B \times \tilde{u}^B|}{||\tilde{u}^B||} \text{sign}(-\tilde{u}_x^B) = \sin(\alpha) \, \text{sign}(-\tilde{u}_x^B),$$

$$L_y^B = \frac{(x^B \cdot \tilde{u}^B)}{||\tilde{u}^B||} \frac{\tilde{u}_y^B}{\sqrt{\tilde{u}_y^{B^2} + \tilde{u}_z^{B^2}}} = \cos(\alpha) \frac{\tilde{u}_y^B}{\sqrt{\tilde{u}_y^{B^2} + \tilde{u}_z^{B^2}}},$$

$$L_z^B = \frac{(p_x \cdot \tilde{u}^B)}{||\tilde{u}^B||} \frac{\tilde{u}_z^B}{\sqrt{\tilde{u}_y^{B^2} + \tilde{u}_z^{B^2}}} = \cos(\alpha) \frac{\tilde{u}_z^B}{\sqrt{\tilde{u}_y^{B^2} + \tilde{u}_z^{B^2}}}.$$

Hence the contribution to particle velocity is given by:

$$\begin{aligned}
\frac{du_L^G}{dt} &= \frac{\frac{1}{2} C_L(Re_p, \alpha) \frac{\pi}{4} d_{eq}^2 \, \rho_f |\tilde{u}^G|^2 R_q^T L^B}{\rho_p \frac{4}{24} \pi \, d_{eq}^3} \\
&= \frac{3 \, C_L(Re_p, \alpha) \, \mu_f \, Re_p}{4 \, \rho_p \, d_{eq}^2} |\tilde{u}^G|^2 R_q^T L^B.
\end{aligned} \tag{13}$$

Particle orientation and calculating torques

As outlined in [17], the angular momentum of a particle, in the body frame and global frame relate to unit Quarternions through the Quarternion matrices $Q(q)$ and $\bar{Q}(q)$ as follows:

$$Q(q) = \begin{bmatrix} q_0 & -q_1 & -q_2 & -q_3 \\ q_1 & q_0 & q_3 & -q_2 \\ q_2 & -q_3 & q_0 & q_1 \\ q_3 & q_2 & -q_1 & q_0 \end{bmatrix},$$

$$\bar{Q}(q) = \begin{bmatrix} q_0 & -q_1 & -q_2 & -q_3 \\ q_1 & q_0 & -q_3 & q_2 \\ q_2 & q_3 & q_0 & -q_1 \\ q_3 & -q_2 & q_1 & q_0 \end{bmatrix}. \tag{14a,b}$$

such that:

$$\dot{q} = \frac{1}{2} Q(q) \begin{bmatrix} 0 \\ \omega_x^G \\ \omega_y^G \\ \omega_x^G \end{bmatrix} = \frac{1}{2} Q(q) \begin{bmatrix} 0 \\ \omega^G \end{bmatrix},$$

$$\dot{q} = \frac{1}{2} \bar{Q}(q) \begin{bmatrix} 0 \\ \omega_x^B \\ \omega_y^B \\ \omega_x^B \end{bmatrix} = \frac{1}{2} \bar{Q}(q) \begin{bmatrix} 0 \\ \omega^B \end{bmatrix}. \tag{15a,b}$$

This is key to solving equation (4). As a particle progresses under the force of the fluid (in the simulation frame of reference), a pitching torque and rotational torque are present. Notably, numerically integrating the Quarternions may lead to them losing their unity, thus they need to be re-normalised after each integration step. For small particles computational errors $O(10^{-16})$ - due to machine precision - may cause numerical instability when solving the angular momentum equations, hence equation (5) must be non-dimensionalised as follows:

Variable	Dimensions
I_p^B	$kg \, . m^2$
$T_P^B(t), T_R^B(t)$	$kg \, . \frac{m^2}{s^2}$
$\omega^B(t)$	$\frac{1}{s}$

$$I_p^{B'} = \frac{I_p^B}{I_{p \, ref}^B}, \qquad I_{p \, ref}^B = m_p d_p^2,$$

$$T_R^{B'} = \frac{T_R^B}{T_{ref}^B}, \qquad T_P^{B'} = \frac{T_P^B}{T_{ref}^B}, \qquad T_{ref}^B = \frac{m_p \, d_p^2 \, L_{ref}^2}{U_{ref}^2},$$

$$\omega_p^{B'} = \frac{\omega_p^B}{\omega_{ref}}, \qquad \omega_{ref} = \frac{L_{ref}}{U_{ref}}.$$

where L_{ref} is the length of the aerofoil chord and U_{ref} the initial velocity of the fluid flow. This yields:

$$\frac{d\omega_p^{B'}(t)}{dt} = I_p^{B'-1} \left(T_P^B(t)' + T_R^B(t)' - \omega_p^{B'}(t) \times \left(I_p^{B'} \omega_p^{B'}(t) \right) \right). \tag{16}$$

Equation (5) continues to hold with the non-dimensionalised angular momentum due to the re-normalisation of the Quarternions and since the Quarternions are dimensionless as seen below:

$$q = \frac{\int \frac{1}{2} \boldsymbol{Q}(q) \begin{bmatrix} 0 \\ \boldsymbol{\omega}^G \end{bmatrix} dt}{\left\| \int \frac{1}{2} \boldsymbol{Q}(q) \begin{bmatrix} 0 \\ \boldsymbol{\omega}^G \end{bmatrix} dt \right\|} = \frac{\frac{U_{ref}}{L_{ref}} \int \frac{1}{2} \boldsymbol{Q}(q) \begin{bmatrix} 0 \\ \boldsymbol{\omega}^{G\prime} \end{bmatrix} dt}{\frac{U_{ref}}{L_{ref}} \left\| \int \frac{1}{2} \boldsymbol{Q}(q) \begin{bmatrix} 0 \\ \boldsymbol{\omega}^{G\prime} \end{bmatrix} dt \right\|}.$$

The pitching torque occurs when the particle's centre of pressure does not coincide with the particle's centre of mass, producing a torque working in the axis perpendicular to the force plane:

$$\boldsymbol{T}_P^{B\prime} = \frac{\frac{1}{4} d_p C_P(Re_p, \alpha) \frac{\pi}{4} d_{eq}^2 \rho_f |\tilde{\boldsymbol{u}}^B| \boldsymbol{P}^B}{\rho_p \frac{4}{3} \pi \left(\frac{d_{eq}}{2}\right)^3 d_p^2 \left(\frac{L_{ref}}{U_{ref}}\right)^2},$$

$$= \frac{3 \, C_P(Re_p, \alpha) \rho_f |\tilde{\boldsymbol{u}}^B| \boldsymbol{P}^B}{8 \, \rho_p \, d_p \, d_{eq} \left(\frac{L_{ref}}{U_{ref}}\right)^2}.$$

(17)

The vector $\boldsymbol{P}^B$ is a unit vector which determines the direction of the pitching torque. Given the axisymmetric shape of the particles about the $\boldsymbol{x}^B$ axis, the contribution of the torque to in the $\boldsymbol{x}^B$ in body space, P_x^B, is always zero. In the $\boldsymbol{y}^B$ and $\boldsymbol{z}^B$ directions the torque is given by:

$$P_y^B = \frac{|\tilde{u}_z^B|}{\sqrt{\tilde{u}_y^{B^2} + \tilde{u}_z^{B^2}}} \operatorname{sign}(\tilde{u}_x^B, \tilde{u}_z^B)$$

(18a)

$$P_z^B = \frac{|\tilde{u}_y^B|}{\sqrt{\tilde{u}_y^{B^2} + \tilde{u}_z^{B^2}}} \operatorname{sign}(\tilde{u}_x^B, \tilde{u}_y^B)$$

(18b)

The rotational torque occurs when the body rotates with respect to the framework of motion, acting to counteract the particle's rotation in proportion to the angular velocity of the particle. Again, since the particle is axisymmetric the torque divides into two components, along the axis of symmetry and perpendicular to it, giving:

$$\boldsymbol{T}_R' = \frac{-\frac{1}{2} \left(\frac{d_p}{2}\right)^5 C_R(Re_R, \alpha) \, \rho_f \, \boldsymbol{R}^B}{\rho_p \frac{4}{3} \pi \left(\frac{d_{eq}}{2}\right)^3 d_p^2 \left(\frac{L_{ref}}{U_{ref}}\right)^2}$$

$$= \frac{-\left(\frac{1}{2}\right)^5 d_p^3 \, C_R(Re_R, \alpha) \, \rho_f \, \boldsymbol{R}^B}{\frac{1}{12} d_{eq}^3 \rho_p \pi \left(\frac{L_{ref}}{U_{ref}}\right)^2}.$$

(19)

The vector $\boldsymbol{R}^B$ is a vector which determines the direction of the rotational contribution and magnitude in relation to the relative angular velocity of the particle and fluid flow: $\boldsymbol{\Omega}^B = \frac{1}{2} \nabla \times \boldsymbol{u}_f^B - \boldsymbol{\omega}_p^B$. Again note that the axisymmetric shape of the particles about the $\boldsymbol{x}^B$ axis provides the similar formula in the $\boldsymbol{y}^B$ and $\boldsymbol{z}^B$ directions:

$$R_x^B = \Omega_x^{B^2}, R_y^B = \Omega_y^B \sqrt{\Omega_y^{B^2} + \Omega_z^{B^2}}, R_z^B = \Omega_z^B \sqrt{\Omega_y^{B^2} + \Omega_z^{B^2}} \quad (20)$$

Furthermore the rotational Reynolds number, Re_R, must be calculated for the formulation of the rotation coefficient C_R:

$$Re_R = \frac{\rho d_p^2 |\boldsymbol{\Omega}^B|}{\mu}$$

In OpenFOAM the curl of the fluid in global co-ordinates can be calculated directly; however, in body co-ordinates the gradient of the fluid velocity must first be found in the global co-ordinates and transformed as follows:

$$* \operatorname{skew}(R_q \nabla \boldsymbol{u}_f^G) = \left((R_q \nabla \boldsymbol{u}_f^G)_{23} - (R_q \nabla \boldsymbol{u}_f^G)_{32}, (R_q \nabla \boldsymbol{u}_f^G)_{31} \right.$$
$$\left. - (R_q \nabla \boldsymbol{u}_f^G)_{13}, (R_q \nabla \boldsymbol{u}_f^G)_{12} - (R_q \nabla \boldsymbol{u}_f^G)_{21} \right)$$

This is the Hodge dual of the skew of the rotated velocity gradient.

When using these torques to solve equation (5) the particle inertia values are required and given in the particle co-ordinate frame by a diagonal matrix since the particles are regularly shaped. To ease input, a non-dimensionalised inertia I'^B is used, such that:

$$I'^B = \frac{I^B}{I_{ref}^B}, \qquad I_{ref}^B = \rho_p \left(\frac{4}{3}\right) \pi \left(\frac{d_{eq}}{2}\right)^3 d_p^2$$

Hence the values of I^B are calculated as follows:

Shape	Inertia values:
Ellipsoid – aspect ratio: w	$I_x = \frac{2}{5} m \left(\frac{d_p}{2w}\right)^2, I_y = I_z = \frac{1}{5} m \left(\left(\frac{d_p}{2w}\right)^2 + \left(\frac{d_p}{2}\right)^2\right)$
Disc – aspect ratio: 5/1	$I_x = I_z = \frac{1}{2} m \left(\frac{d_p}{2}\right)^2, \qquad I_y = m \left(\frac{d_p}{2}\right)^2$
Cylinder – aspect ratio: 5/1	$I_x = \frac{1}{2} m \left(\frac{d_p}{2}\right)^2, \qquad I_y = I_z = \frac{1}{12} m \left(3 \left(\frac{d_p}{2}\right)^2 + \left(\frac{d_p}{10}\right)^2\right)$

Taking equations (3), (5) and (15a) together gives a 10 ODE system that needs to be solved for this fluid-particle system – three pertaining to the particle velocity, three to the particle angular momentum and four to solve the change in the Quarternions.

Computational method and results

There are two stages to solving this uncoupled system i.e. any influence of the particle on the fluid is ignored. Firstly, the aerodynamic flow around the aircraft is calculated using the SIMPLE (Semi-Implicit Method for Pressure-Linked Equations) algorithm to solve the Navier-Stokes equations for the steady-state flow of an incompressible fluid with turbulence modelling [20]. Once the continuous phase solution has been obtained, the particle trajectory solution is calculated. Using a Lagrangian method, each particle's location, orientation, and velocity is calculated as above and updated over several time steps.

Each particle's initial location, orientation and velocity are input by the user. The initial release location is set far away from the aerofoil for each particle and their initial velocities are set equal to the free-stream flow condition. The initial angular velocity is set to zero. This is reasonable since the particle's rotation is driven by the aerodynamic torques and forces hence placing it far enough downstream will cause the particles to rotate under the fluids action and ensure an almost constant angular velocity in the free stream. Furthermore the particle's x-axis is aligned with direction of U_{rel}.

For comparison four correlations laws are used. Firstly, a drag-only sphere law that is applied as standard in OpenFOAM is applied to each scenario for comparison as to how the trajectories of different shaped particles deviate from a spherical assumption. Secondly, for comparison with another widely used methods, results for a non-spherical drag law by [21], denoted G-model, where non-spherical particles are parameterized by sphericity, is implemented. There are several possible choices for such models discussed in [12]. Ultimately the model derived by Ganser was chosen since previous analysis shows that there can often be little difference between the results of such correlations [22], hence this is representative of correlations based on sphericity. Thirdly and

fourthly, as noted earlier the full rotational models developed in [7] and [16]. The particle shapes discussed in [7] are used for comparative analysis. The aim is to identify benefits and limitations of the fully rotational approaches denoted Z-model [7] and W-model [16].

Catch efficiency

A local collection efficiency, β, is calculated to assess the difference that particle shapes make to the impingement of particles across the aircraft geometry. This parameter is a ratio of the area spanned by the particles in the free stream A_0 and the area that the particles span having impinged on the geometry A_h. When the angle-of-attack $\alpha > 0$, the initial area spanned by the particle's are projected in the plane perpendicular to the oncoming flow, such that:

$$\beta = \frac{A_0 \cos(\alpha)}{A_h}$$

In calculating this parameter for a range of particle shapes and sizes, difference in the particle trajectories, particularly how they respond to the evolving airflow about the aircraft, has on the impact location.

Runge Kutta vs Forward Euler

To implement the above correlations, a numerical scheme must be chosen to integrate each force and torque equation in time and thus compute each particle's trajectory. Given the increased number of equations required to model the full rotational dynamics the solution to this system will already be of greater cost than a drag-only model. Yet there is a further inherent trade-off between running time and numerical accuracy in the choice of numerical scheme that needs to be managed. Here two common choices of scheme are compared - a fourth order Runge-Kutta (RK) scheme and a Forward Euler scheme.

The fourth order RK scheme, whilst known to be more accurate, is computationally more intense. Thus, the maximum allowable time step that provides an acceptable threshold of accuracy is now investigated. Notably, the airspeed here is $80 ms^{-1}$. This is important since the accuracy of the time step is likely to be speed dependent. In addition, it is also likely to vary with pressure gradients. As a result, the range of dt investigated now is of relevance to this case and may need to be investigated directly for other scenarios in response to different velocity profiles and additional factors such as the size of the velocity gradients.

Figure 4 presents a comparison between the implementation of a Forward Euler scheme in comparison to a fourth order RK solution with a significantly smaller time step. The example shown is the catch for $20\mu m$ Ellipsoids of aspect ratio $w = 2.5$ on the main element of a three-element high lift aerofoil. Through numerical experimentation and observation, the results for this region were found to be the most sensitive to the choice of scheme and size of time step. Issues are clearly seen for $\delta t \geq 0.00001$ with the Forward Euler scheme failing to capture the maximum catch value and its location. Likewise, further resolution issues are seen after this peak in the negative s direction. Thus, in the presented scenarios the maximum time step used is $\delta t = 0.000005$.

In Figure 5, comparisons for the fourth order Runge-Kutta scheme with varying time step are presented for the same scenario as above. As δt decreases the solutions tend towards that of $\delta t = 0.0000025$, matching closely for $\delta t = 0.00001$ (notably the dark blue curve for $\delta t = 0.0000025$ is matched by the red and yellow curves). Hence for the fourth order Runge-Kutta scheme a smaller time step may be used to provide an accurate result. The question which now remains is how the running time of these two schemes for a range of scenarios compare.
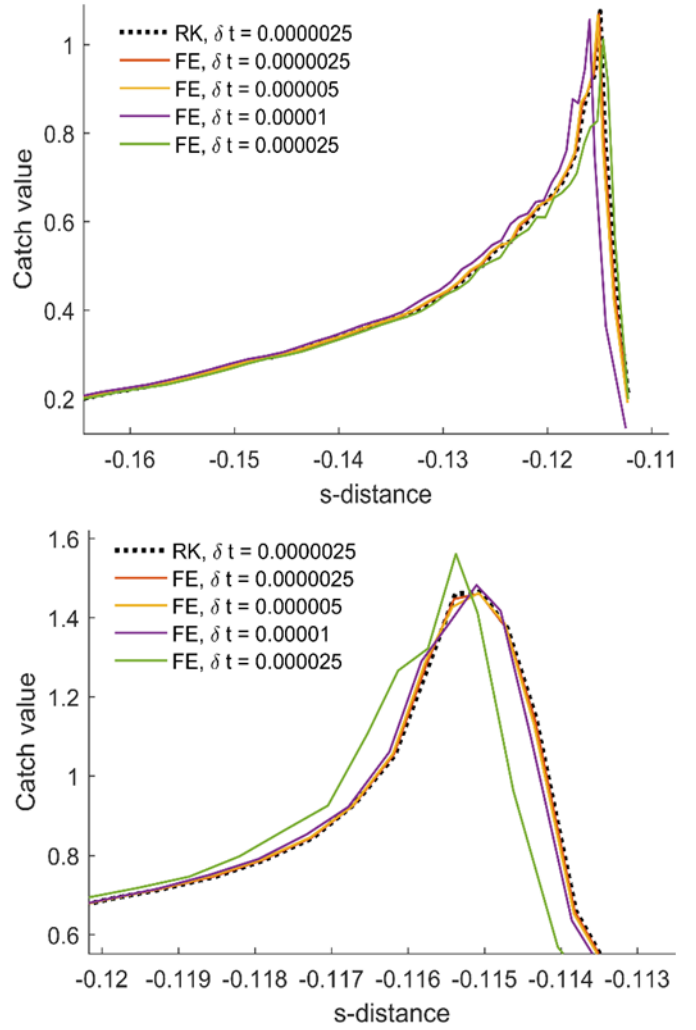

Figure 4: Computational results comparing solution using Forward Euler with varying time step to the fourth order Runge-Kutta solution at $\delta t = 0.0000025$ for main element of a three-element high lift aerofoil. Top: [7], Bottom: [16].

In table 2 the computational speed of each correlation and numerical scheme is calculated relative to the spherical drag law case, using OpenFOAM's forward Euler scheme. For the full rotational models, denoted Z [7] and W [16], the relative time for the two schemes is shown. Furthermore, maximum errors and average errors are computed in each case, for each full rotational model. The error is given in comparison to the fourth order RK results with $\delta t = 0.0000025$, denoted by the subscript B. The formula for error calculation are:

$$\text{Max error: } \max_{i} \left(\frac{\beta_{C,i} - \beta_{B,i}}{\beta_{B,i}}^2 + \frac{s_{C,i} - s_{B,i}}{s_{B,i}} \right)^{\frac{1}{2}}$$

$$\text{Average error: } \frac{1}{n} \sum_{i}^{n} \left(\frac{\beta_{C,i} - \beta_{B,i}}{\beta_{B,i}}^2 + \frac{s_{C,i} - s_{B,i}}{s_{B,i}} \right)^{\frac{1}{2}}$$

	$S, \delta t_1$	$G, \delta t_1$	$Z, FE, \delta t_1$	$Z, RK, \delta t_2$	$W, FE, \delta t_1$	$W, RK, \delta t_2$
Relative time	1	1.35	2.54	3.79	3.13	4.86
Max error	N/A	N/A	10.77%	3.34%	3.90%	0.43%
Average error	N/A	N/A	13.36%	3.55%	5.31%	0.68%

Table 2: Comparison of relative running times to the spherical case and accuracy compared to $\delta t = 0.0000025$ case of each correlation model for different numerical schemes. $\delta t_1 = 0.000005$, $\delta t_2 = 0.00001$, S: sphere drag, G: [21], Z: [7], W: [16].
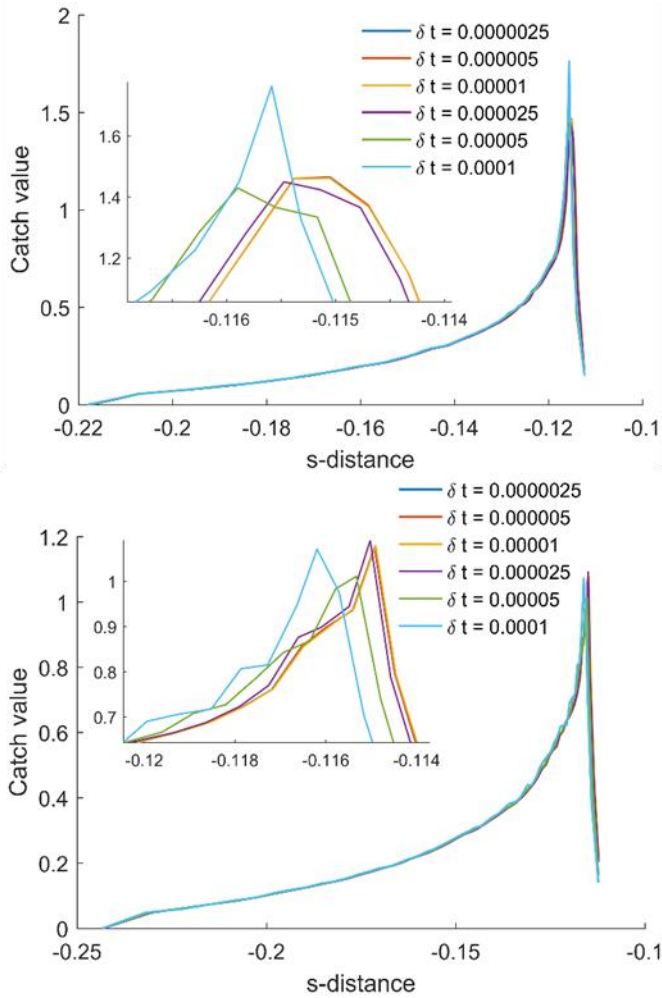
Figure 5: Computational results comparing solution using Forward Euler with varying time step to the fourth order Runge-Kutta solution at $\delta t = 0.0000025$ for main element of a three-element high lift aerofoil. Top: [7], Bottom: [16].

By inspection of the numerical results and the above error analysis, the Runge Kutta scheme is used in the following analysis for the full rotational models with $\delta t = 0.00001$ whilst the forward Euler scheme is implemented for the drag only cases with $\delta t = 0.000005$.

Results

Presented are two configurations – each originally modelled in [23] - to illustrate the methods. The cases presented are not validation cases rather they serve as an illustration of the analysis and the difference seen in using different correlations to model particles of varying shape and size. This is to aid discussion as to how this analysis may be used. Whilst ice crystal impingement is not of significant concern for aerofoils the varying geometries serve as helpful examples of how each method differs in terms of the effect on the trajectory.

To ensure that the results are comparable, each shaped particle is characterised by a volume equivalent diameter - the diameter for a spherical particle that has the same volume and thus same mass as the modelled particle

NACA0012

The first test case is for a symmetric NACA0012 aerofoil. At zero degrees angle of attack, the free-stream flow is set to $\dot{x}_{ref} = 80 ms^{-1}$ with a 1m chord. Analysis is run for a range of particle shapes, given in [7]. Two sizes of particle are modelled, relating to volume equivalent spheres with diameters $d_{eq} = 20\mu m$ and $d_{eq} = 100\mu m$. Figure 6 shows the velocity profile over the aerofoil.
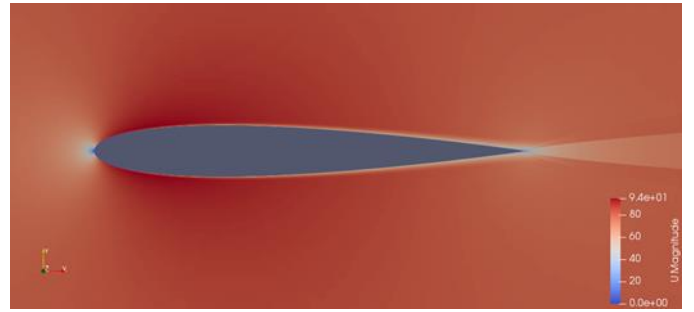

Figure 6: Computational result for the velocity profile over the NACA0012 aerofoil at 0° angle-of-attack.

The catch efficiency over s, the wrap distance from the leading edge, is presented in Figure 8, for particles equivalent to a $20\mu m$ sphere, and in Figure 9, for particles equivalent to a $100\mu m$ sphere. Notably, for the larger particles there is less of a difference between each shape in both the catch and the extent to which the particles impinge – other than for disc-like particles. This is the case for each correlation. The reason for this is due to larger particles possessing a more ballistic trajectory such that they are less responsive to the changes in pressure about the aerofoil and the profile of the airflow around the symmetric aerofoil. For the $20\mu m$ particle case, there is a clear difference in the catch of each particle with the disc-type particle having a greater catch at the leading edge yet having a smaller extent for the full rotational model. This is due to their geometry, since once aligned with the flow they follow it more closely than the other particle shapes.

Already issues with the drag only law based on sphericity can be seen. Despite the simple geometry and symmetry of the aerofoil, the catch is almost the same for both the cylindrical particle and the disc-type particle, for both sizes. It is widely expected [12] [23] that their response to the airflow should be quite different, yet this is not captured here. Additionally, in this simple example the full rotational model presented in [16] shows little variation between the different shaped particles, irrespective of size. Notably however this is also seen in the case of the other correlations, with the results for the ellipsoid particles all being of similar extent and order of magnitude over the leading edge.

Three element high-lift aerofoil

The second case relates to the L1T2 three element high-lift aerofoil [24]. At an angle of attack of 4°, the freestream velocity is $80\ ms^{-1}$ and 1 m chord. This case is of greater complexity geometrically in terms of the flow field about the aerofoil, Figure 7. In this case, due to the design of the aerofoil, high circulation in the air flow is possible with a strong interaction occurring between the fluid flow and particles in both cases [23]. In Figures 10, 11 and 12 the catch across each of the three sections is presented, plotted against the wrap distance, s, over each section.
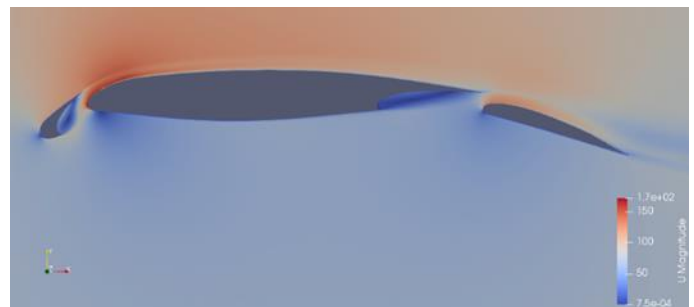

Figure 7: Computational result for the air velocity profile over a three element high-lift aerofoil at 4° angle of attack.

Beginning with the leading-edge section, the slat, a significant difference is seen in the catch and extent according to the correlation used and size of the particle. In the $20\mu m$ case, Figure 10a, the disc-type and cylindrical particles both have the lowest peak catch across the slat.
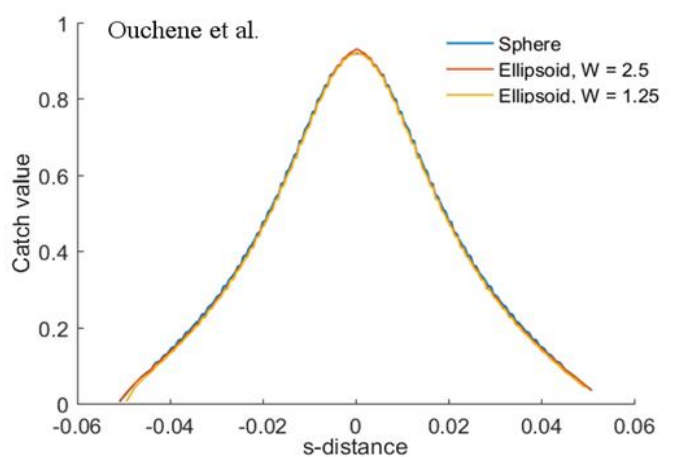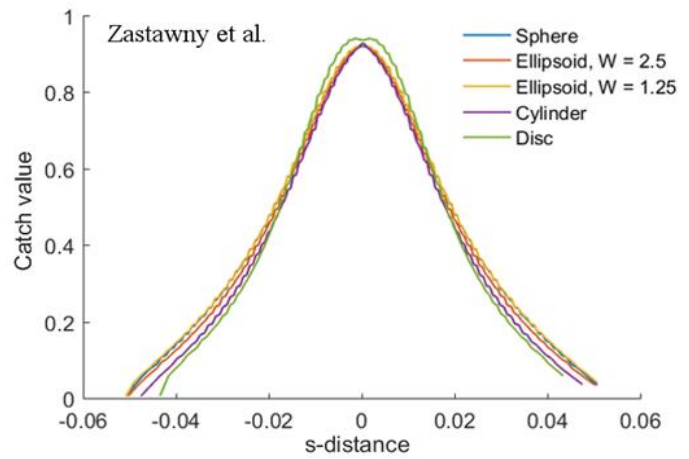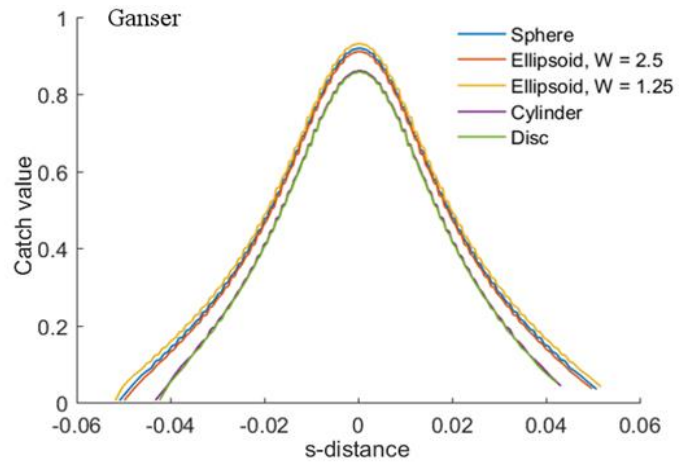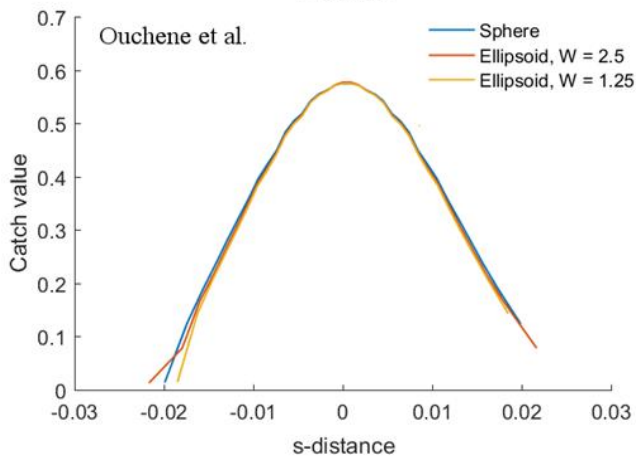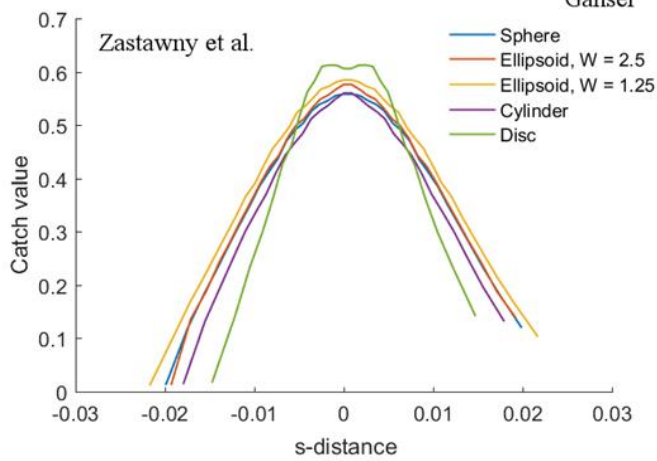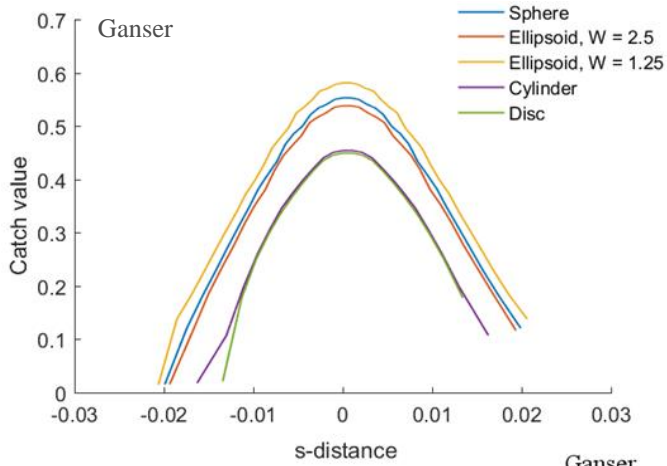
Figure 8: Catch result β for the NACA0012 aerofoil at 0° angle of attack for particles of $d_{eq} = 20\mu m$. Top: [21], Middle: [7], Bottom: [16].

Figure 9: Catch result β for the NACA0012 aerofoil at 0° angle of attack for particles of $d_{eq} = 100\mu m$. Top: [21], Middle: [7], Bottom: [16].

The full-rotational Z-model shows a lower extent for the disc, whilst the non-spherical drag only G-model provides very similar results for the cylindrical and disc-type particles. For the $100\mu m$ case, Figure 10b, with the full rotational Z-model gives a significantly greater extent and catch further aft for cylindrical particles compared to the G-model, yet a similar result for the disc-type ones. Regarding the ellipsoidal particles, the two full rotational models corroborate well throughout, whilst the drag only G-model gives a markedly lower catch result for an ellipsoid of aspect ratio $w = 2.5$.

Next, over the main element a similar trend is seen for the $20 \mu m$ particles, Figure 11a. Notably, for this case there is a significant enhancement region due to the particle concentration around the slat. When full rotational dynamics are modelled, the disc-type and cylindrical particles have lower peak catches yet the discs

possess a far larger extent. Likewise, the peak catch for the ellipsoidal particles differ greatly with each less than the spherical case. Whilst the full rotational Z-model differs from the drag only case, both full rotational models provide similar results. Notably, in general the smaller particles do not impinge far down the main element, mostly keeping towards the leading edge. For the $100\mu m$ particles the extent is far greater with a lower catch efficiency due to the more ballistic trajectories of the larger particles, Figure 11b. Overall, with full rotational dynamics the disc-type and cylindrical particles possess a higher catch throughout the main element region, and possess a similar peak catch at the leading edge. Notably, each non-spherical shape has a slightly higher catch than the sphere under full rotation and both the Z-model and W-model corroborate. The drag only G-model once again has a far smaller catch and extent for each shape. In fact, the peak catch is simply shifted from the sphericity model as, from a drag point of view, they are essentially smaller particles that have different inertial separation.
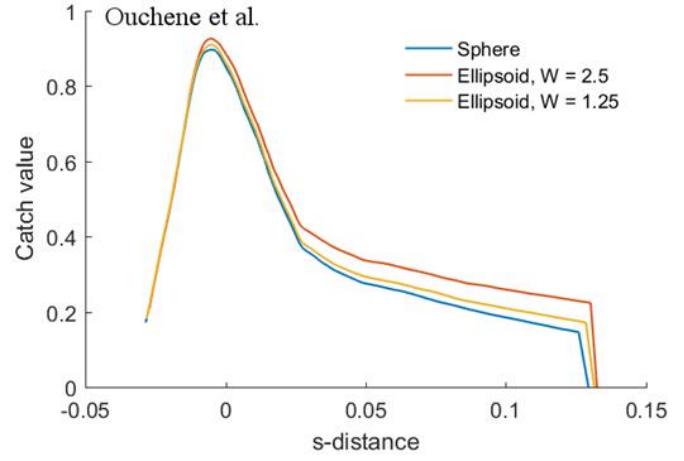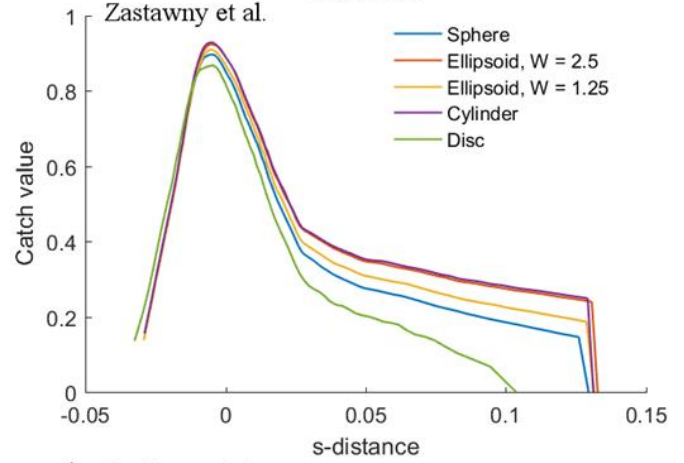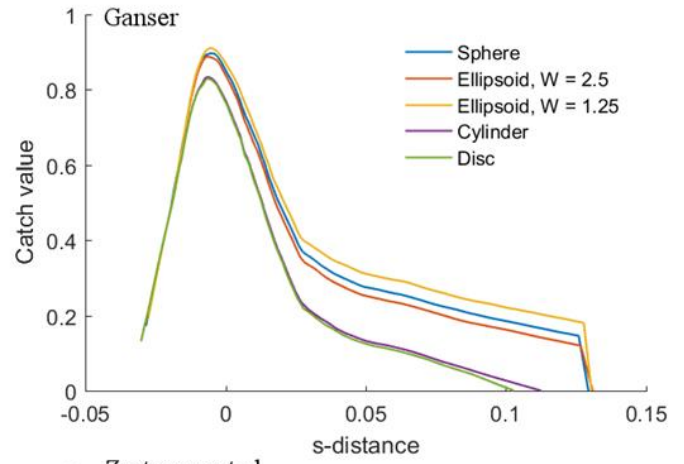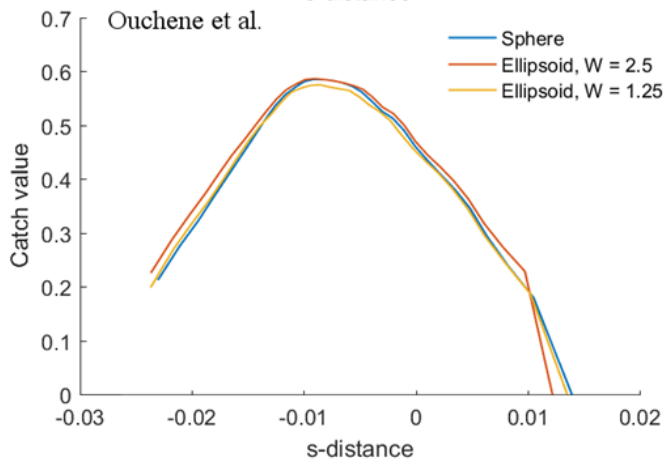
Figure 10a: Catch result β over the front slat for the three element high-lift aerofoil at 4° angle of attack for particles of $d_{eq} = 20\mu m$. Top: [21], Middle: [7], Bottom: [16].
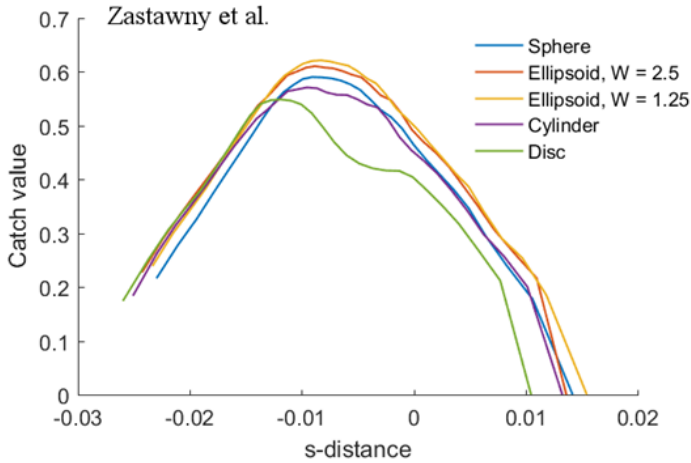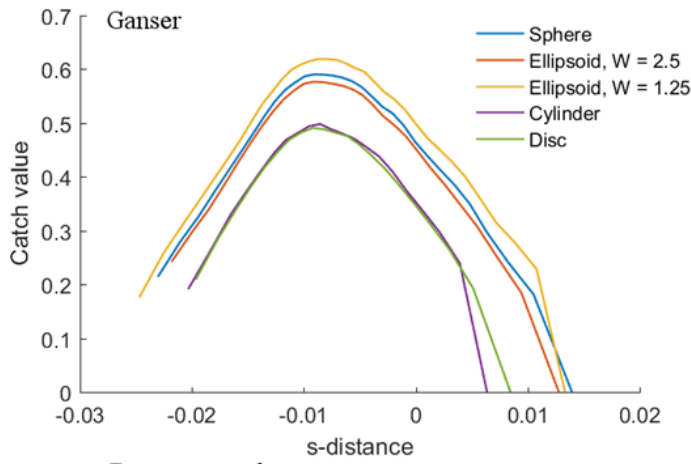

Figure 10b: Catch result β over the front slat for the three element high-lift aerofoil at 4° angle of attack for particles of $d_{eq} = 100\mu m$. Top: [21], Middle: [7], Bottom: [16].

Finally, across the flap several key features are seen. For the $20\ \mu m$ case, Figure 12a, the peak catch is located at the leading edge of the flap. Each particle has different peak catch value, each differing between the Z-model and the G-model. For the full rotational Z-model the extent is similar for each particle other than the disc, which has a greater coverage. For the $100\mu m$ case, Figure 12b, the same trends seen previously are again shown with the full rotational models producing a higher catch further aft. The drag only case gives notably different results for both peak catch and extent to the two full rotational models (which otherwise agree). For both particle sizes, the disc-type particles are similar for both the G-model and the Z-model, yet the cylindrical particles are significantly different.

Discussion

Overall, each particle shape gives different catch results when compared to the spherical case. For the larger particles the shape has a more significant effect on the results. Furthermore, the difference between the full rotational model and drag only case is greater when the particles are larger with both full dynamic models showing agreement for the ellipsoidal particles. The disc-type and cylindrical type particles each portray unique characteristics and results for the full dynamics, potentially highlighting a weakness in the sphericity-based model. Regarding the use of these methods for industrial analysis, running both a sphere case and a disc case likely covers most of the range of interest.
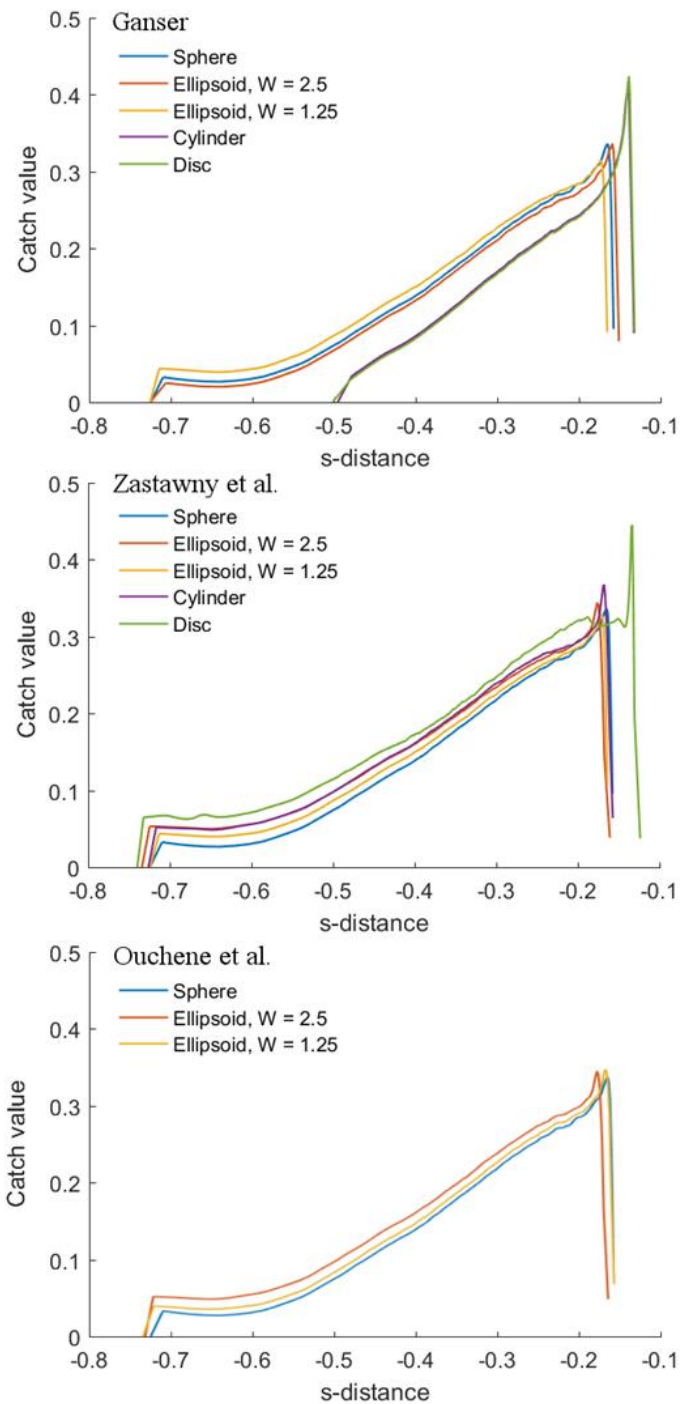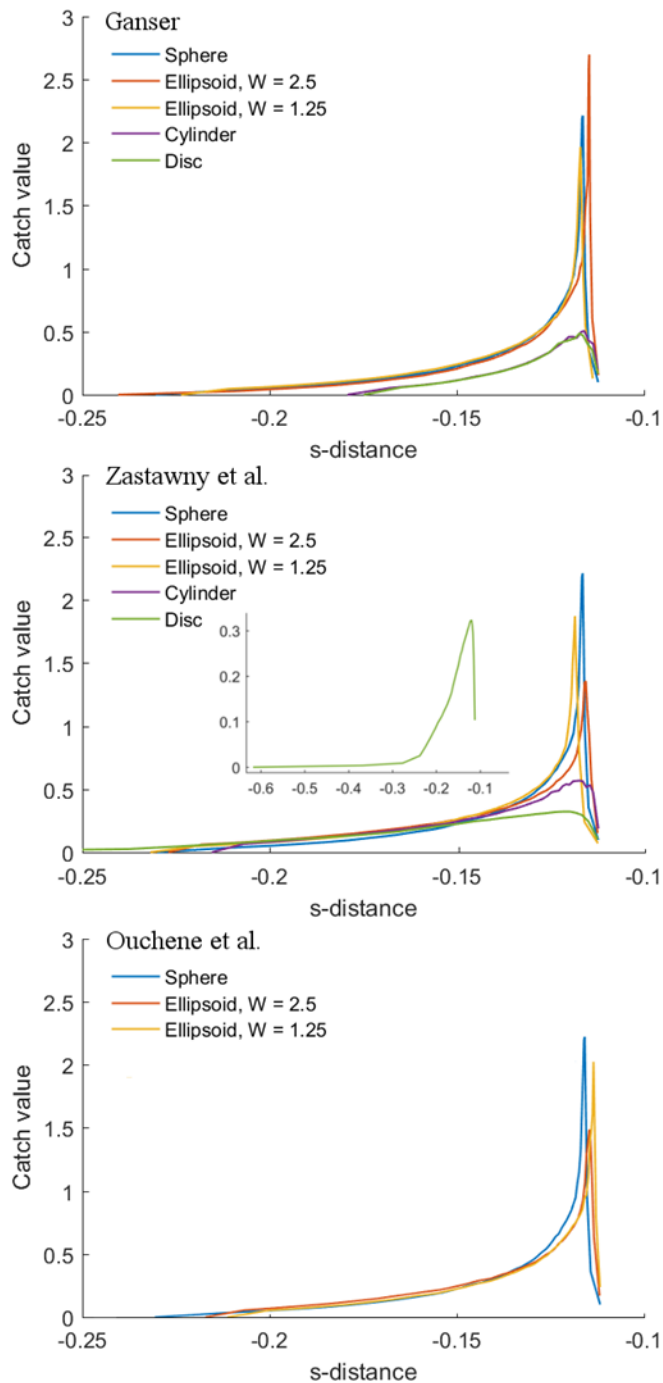
Figure 11a: Catch result β over the main element for the three element high-lift aerofoil at 4° angle of attack for particles of $d_{eq} = 20\mu m$. Top: [21], Middle: [7], Bottom: [16].

Figure 11b: Catch result β over the main element for the three element high-lift aerofoil at 4° angle of attack for particles of $d_{eq} = 100\mu m$. Top: [21], Middle: [7], Bottom: [16].

Of note, the sphericity model produces significantly different results when the bodies themselves are significantly different from a spherical shape. A more sophisticated model such as that of Holzer and Sommerfield [14] may capture these differences, however previous analysis show that results can be similar to the Ganser drag [22] and that it possess its on difficulties and inaccuracies when calculating the two types sphericity [12].

Whilst ice crystals are not of significant issue to aerofoils, overall these results indicate that from an engineering point of view, users need to be aware of the range of impingement that may occur. This is in terms of both its extent and the level for a range of different particle shapes to ensure that the design is robust to a range of conditions. This is especially true for complex geometries and airflow given that different

shapes have different impingement ranges, for similar masses, over different sections.

Hence, the above results show that when assessing engine impingement limits, care must be taken to account for differences in both the extent and level of impingement – particularly significance of disc-type particles. Similar attention must be paid to the impingement of Ellipsoid 2 particles, that have a higher extent of catch than the equivalent sphere and therefore may require a greater protection area or require alternative design procedures for engine geometries. Furthermore, in the L1T2 aerofoil case there appears to be a significant difference in the enhancement region on the main aerofoil. This is an area that would require further investigation. However, initially this highlights
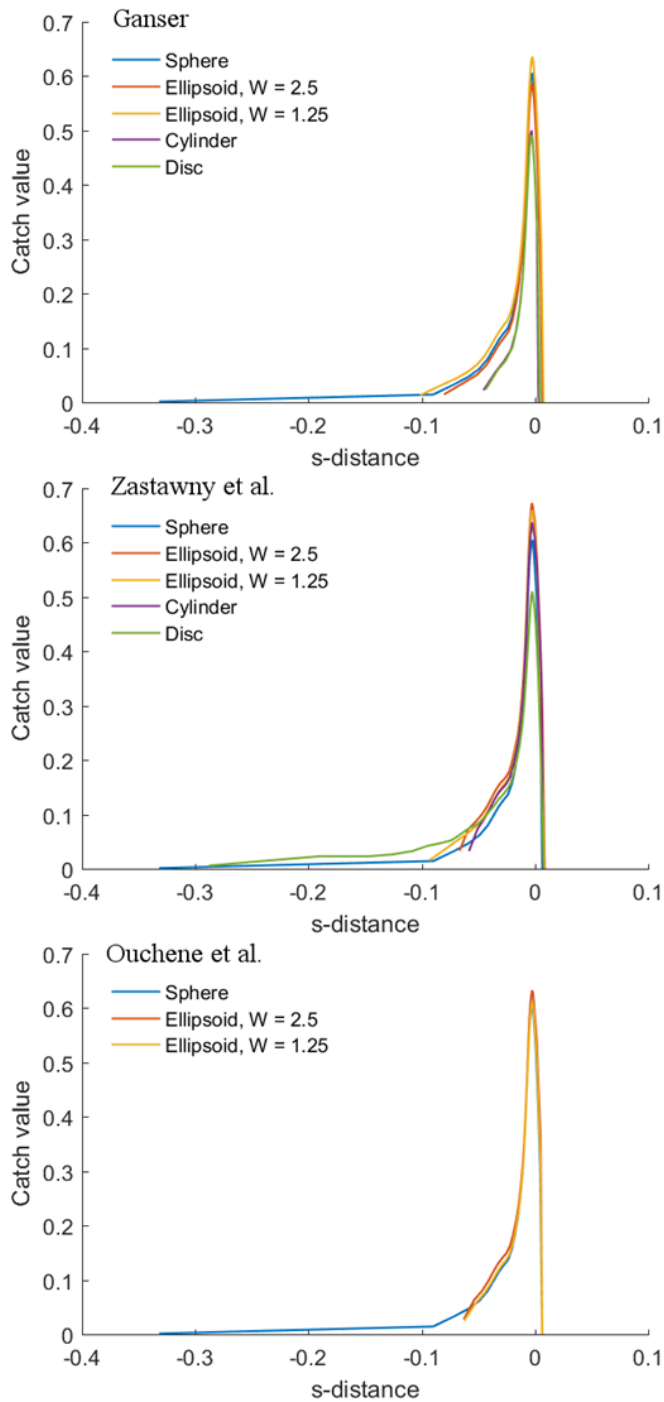
Figure 12a: Catch result β over the rear flap for the three element high-lift aerofoil at 4° angle of attack for particles of $d_{eq} = 20\mu m$. Top: [21], Middle: [7], Bottom: [16].

Figure 12b: Catch result $\boldsymbol{\beta}$ over the rear flap for the three element high-lift aerofoil at $\mathbf{4°}$ angle of attack for particles of $\boldsymbol{d_{eq} = 100\mu m}$. Top: [21], Middle: [7], Bottom: [16]

a particularly important issue for engines where there are a numbers of rotors and stators where enhancement/deficit regions may occur – hence careful modelling of different shaped particles is of increasing need and benefit.

The implementation of this method has several benefits. Firstly, it allows for analysis of a wider range of ice shapes that are commonly seen in icing conditions [8]. Providing four different shapes, these cover the general scope of particles seen in practice and capture the dynamics and behaviours specific to these particles. Previously, drag, lift and torque coefficients have been dependent on the measure of sphericity for particles. Whilst this provides greater flexibility, it fails to capture the nuances of different shaped particles trajectories and rotation
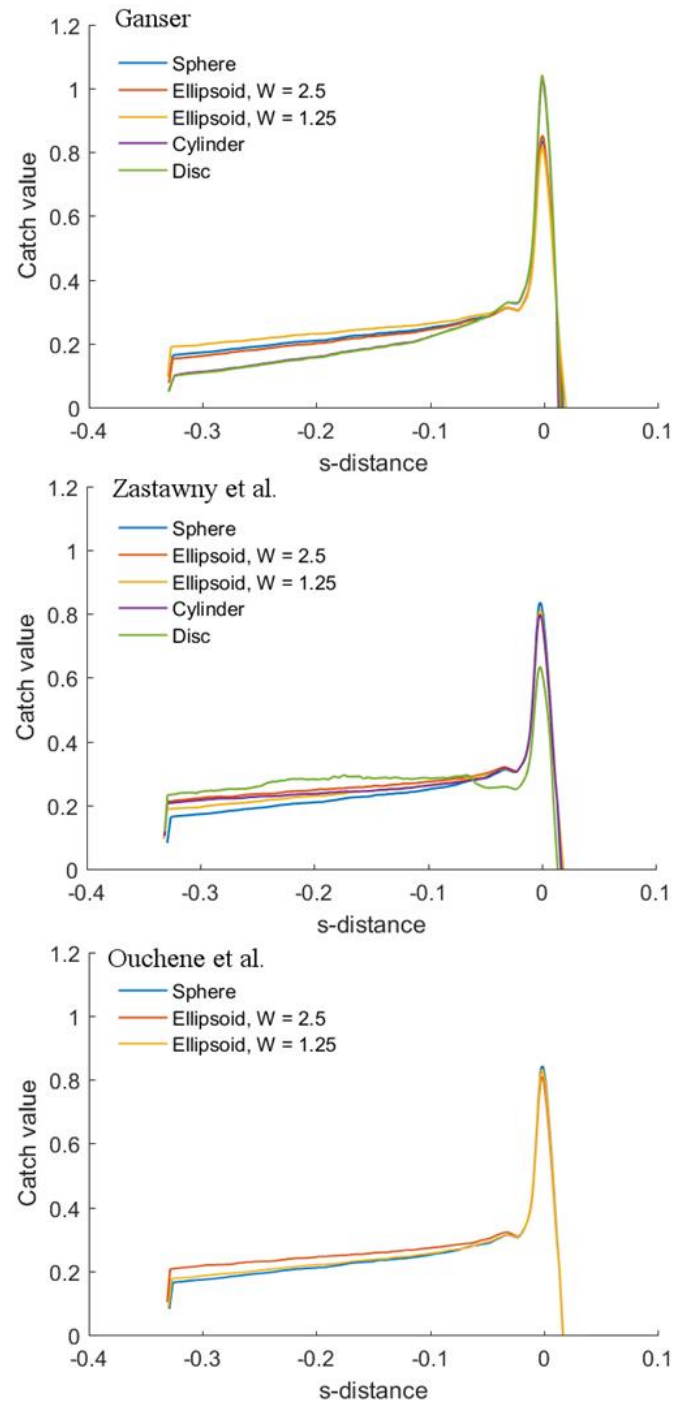
– in particular, the pressure response about them. Likewise, particles of significantly different shape could be characterised by the same sphericity, leading to specific shape effects for different particles to be ignored. It should also be noted that there are several methods for calculating the drag and lift on non-spherical particles, based on sphericity, of which there is often no clear best practice [22]. Furthermore, to calculate the torque, the centre of mass for the particle was previously required; however, again there was no clear method that was best [12]. Both issues are avoided.

Secondly, the method provides an opportunity for new analysis – the creation of catch bounds for mixed clouds. As seen in the analysis section, taking the worst- and best-case scenarios provides a range of values for the catch, which can help to better understand the extent to

which particles impinge and where. This is pertinent for smaller particles whose trajectories are more effected by the pressure gradient over the aircraft and larger particles where the shape was shown to have a bigger influence. Hence a catch-limit for a mixed cloud of particles, perhaps of different shaped particles and different sized particles, may be easily gained. It is worth noting that since each particle is modelled as having the same mass, it is their aerodynamic differences and response that are driving the differences in catch. Generally, the results of this investigation have shown that the differences in shape as well as the size of particles are important in determining the catch value and impingement range.

Limitations

Despite the benefits, there are several limitations. Firstly, since the method is formulated for prescribed particle shapes there is a lack of flexibility in the particles that may be analysed. This is an issue that is common to correlation approaches since the formulae are often gained through matching curves/functions to data points from experiments or simulations [12]. As a result, the models may only be applied for very specific scenarios and values, as seen in this paper. Despite these limitations, the methods still apply to icing scenarios as the parameters are within the correct state space and thus these methods are of benefit.

Secondly, the implemented method is slower than that of the spherical particles. Running times increase due to the increased number of numerical operations required for the fourth order Runge-Kutta and the additional ODEs provided by the orientation tracking greatly affect the running time. Hence, there is a trade-off. Since the results show significant difference, there is a benefit to running these scenarios when considering ice crystals; however, since five particle shapes are considered the running time is further increased.

Finally, as noted earlier, the difficulties in experimentation and lack of experimental data create a further limitation. To be used industrially, the method must be shown to be accurate and reliable under a range of icing scenarios and requires validation which is not easily carried out at the moment, especially when specific shapes are considered. This limitation may not be such an issue however when considering a mixed cloud of particles or the use of the method for worst- and best- case scenario analyses. Additionally, the derivation of the full rotational models is based on highly physical DNS which may help to provide further confidence in the accuracy of these methods. However, this is not sufficient to replace the need for validation.

Future work

A natural next step is to understand better the impingement of different shaped particles based on their velocity, angle of incidence to the flow, angle of impact and their angular rotation. There are several studies that have looked at these dynamics for different shaped particles (e.g. [24], [19]). With this, particle melting, and the effect of liquid layers would also be of benefit when assessing icing encounters related to engines or heated instruments such as pitot tubes.

As stated in the limitations section, experimentation is also an important next step particularly datasets from impingement experiments that can record each particles size, general shape and impingement location. This would help to further refine the work and identify other limitations.

Conclusions

The present work has investigated new methods for modelling and analysing aircraft icing in the case of ice crystals. The results of two models which calculate the trajectory, orientation and rotation of various shaped non-spherical particles have been compared to a drag only models. This is a non-coupled method whereby an aerodynamic solution is first computed at steady-state, after which a cloud of particles is released and tracked to impact on the aircraft. Previously, within the

range of Reynolds number permitted in this study, it was only possible to model the trajectory and full rotational progression of cylindrical particles.

Incorporating these new capabilities into the modelling of aircraft icing opens new avenues for industrial analysis. Specifically, upper and lower bounds can be gained for the catch of particles on relevant aircraft geometries. This is helpful in increasing knowledge of how icing occurs in an ice crystal environment by considering ice particles that come in many different shapes and sizes. In turn this may benefit several areas of design for aircraft engine geometries and ice protection systems as well as other components prone to ice crystal accretions.

Contact Information

Ryan Palmer, Ph. D.
Affiliation: Department of Mathematics, University College London
e-mail: ryan.palmer.14@ucl.ac.uk

Acknowledgements

References

[1]   NTSB, 2011. [Online]. Available: https://www.ntsb.gov/news/speeches/EWeener/Documents/weener_020111.pdf.

[2]   FAA, "Federal Regulations," September 2018. [Online]. Available: https://www.ecfr.gov/cgi-bin/text-idx?c=ecfr&tpl=/ecfrbrowse/Title14/14tab_02.tpl.

[3]   J. Mason, W. Strapp and C. Philip, "The ice particle threat to engines in flight," *44th AIAA Aerospace Sciences Meeting and Exhibit,* 2006.

[4]   Bureau d'Enquêtes et d'Analyses, "Final report on the accident on 1st June 2009 to the Airbus A330-203 registered F-GZCP operated by Air France flight AF 447 Rio de Janeiro–Paris," Paris: BEA, 2012.

[5]   C. Tropea, E. Bonaccurso, A. Criscione, T. Hauk, S. Jakirlic, D. Kintea, H. Li, I. V. Roisman and M. Schremb, "Physics of aircraft icing: A predictive challenge," in *ICHMT DIGITAL LIBRARY ONLINE*, 2015.

[6]   R. Gent, N. P. Dart and J. T. Cansdale, "Aircraft icing," *Philosophical Transactions of the Royal*

Society of London A: Mathematical, Physical and Engineering Sciences, 2000.

[7]   M. Zastawny, G. Mallouppas, F. Zhao and B. van Wachem, "Derivation of drag and lift force and torque coefficients for non-spherical particles in flows," *International Journal of Multiphase Flow,* pp. 227-239, 2012.

[8]   R. P. Lawson, B. Baker, B. Pilson and Q. Mo, "In Situ Observations of the Microphysical Properties of Wave, Cirrus, and Anvil Clouds. Part II: Cirrus Clouds," *Journal of the Atmospheric Sciences,* vol. 63, no. 12, pp. 3186-3203, 2006.

[9]   S. A. Orszag, "Analytical theories of turbulence," *Journal of Fluid Mechanics,* 1970.

[10] R. Begum and M. A. Basit, "Lattice Boltzmann method and its applications to fluid flow problems," *European Journal of Scientific Research,* 2008.

[11] S. Wagner, "Computational Fluid Dynamics," in *High Performance Computing in Science and Engineering*, Springer, 2008.

[12] M. Mandø and L. Rosendahl, "On the motion of non-spherical particles at high Reynolds number," *Powder Technology,* 2010.

[13] H. Wadell, "The coefficient of resistence as a function of Reynolds number for solids of various shapes," *Journal of the Franklin Institute,* 1934.

[14] A. Holzer and M. Sommerfield, "New simple correlation formula for the drag coefficient of non-spherical particles," *Powder Technology,* 2008.

[15] A. Holzer and M. Sommerfield, "Lattice boltzmann simulations to determine, lift and torque acting on non-spherical particles," *Computers and Fluids,* 2009.

[16] R. Ouchene, M. Khalij, B. Arcen and A. Tanière, "A new set of correlations of drag, lift and torque coefficients for non-spherical particles and large Reynolds numbers," *Powder Technology,* vol. 303, pp. 33-43, 2016.

[17] B. Kenwright, "A beginners guide to dual-quaternion," in *20th WSCG International Conference*, Plzen, 2012.

[18] L. Ibanez, "Tutorial on quaternions part I," *Insight Segmentation and Registration Toolkit (ITK),* 2001.

[19] B. van Wachem, M. Zastawny, F. Zhao and G. Mallouppas, "Modelling of gas-solid turbulent channel flow with non-spherical particles with large Stokes number.," *International Journal of Multiphase Flow,* pp. 80-92, 2015.

[20] S. V. Patankar and B. D. Spallding, "A calculation procedure for heat, mass and momentum transfer in three-dimensional parabolic flows.," *Numerical Prediction of Flow, Heat Transfer, Turbulence and Combustion,* pp. 54-73, 1983.

[21] G. H. Ganser, "A rational approach to drag prediction of spherical and nonspherical particles," *Powder Technology,* vol. 77, no. 2, pp. 143-152, 1993.

[22] E. Norde, "Eulerian method for ice crystal icing in turbofan engines," University of Twente, 2017.

[23] M. Widhalm, "Lagrangian Trajectory Simulation of Rotating Regular Shaped Ice Particles," in *SAE Technical Paper*, 2015.

[24] "ERCOFTAC Knowledge Base Wiki," [Online]. Available: http://www.kbwiki.ercoftac.org/w/index.php/Description_AC1-08. [Accessed March 2019].

[25] M. Allen, D. Frenkel and J. Talbot, "Molecular dynamics simulation using hard particles," *Computer Physics Reports,* pp. 301-353, 1989.

Appendices

Correlations from [7] for full rotational particle trajectories.

For $Re_p \leq 300$.

Drag: $C_D(\alpha) = C_{D,0} + \left(C_{D,\pi/2} - C_{D,0}\right)\sin^{a_0}\alpha$, $C_{D,0} = \frac{a_1}{Re^{a_2}} + \frac{a_3}{Re^{a_4}}$, $C_{D,\pi/2} = \frac{a_5}{Re^{a_6}} + \frac{a_7}{Re^{a_8}}$,

Coefficient	Ellipsoid (5/2)	Ellipsoid (5/4)	Disc	Cylinder
a_0	2.0	1.95	1.96	2.12
a_1	5.1	18.12	5.82	20.35
a_2	0.48	1.023	0.44	0.98
a_3	15.52	4.26	15.56	2.77
a_4	1.05	0.384	1.068	0.396
a_5	24.68	21.52	35.41	29.14
a_6	0.98	0.99	0.96	0.97
a_7	3.19	2.86	3.63	3.66
a_8	0.21	0.26	0.05	0.16

Lift: $C_L = \left(\frac{b_1}{Re^{b_2}} + \frac{b_3}{Re^{b_4}}\right)\sin^{b_5+b_6 Re^{b_7}}(\alpha)\cos^{b_8+b_9 Re^{b_{10}}}(\alpha)$,

Coefficient	Ellipsoid (5/2)	Ellipsoid (5/4)	Disc	Cylinder
b_1	6.079	0.083	12.111	8.652
b_2	0.898	-0.21	1.036	0.815
b_3	0.74	1.582	3.887	0.407
b_4	-0.028	0.851	0.109	-0.197
b_5	1.067	1.842	0.812	0.978
b_6	0.0025	-0.802	0.249	0.036
b_7	0.818	-0.006	-0.198	0.451
b_8	1.049	0.874	5.821	1.359
b_9	0.0	0.009	-4.717	-0.43
b_{10}	0.0	0.57	0.007	0.007

Pitching Torque: $C_T = \left(\frac{c_1}{Re^{c_2}} + \frac{c_3}{Re^{c_4}}\right) \sin^{c_5 + c_6 Re^{c_7}}(\alpha) \cos^{c_8 + c_9 Re^{c_{10}}}(\alpha)$,

Coefficient	Ellipsoid (5/2)	Ellipsoid (5/4)	Disc	Cylinder
c_1	2.078	0.935	3.782	0.011
c_2	0.279	0.146	0.237	-0.656
c_3	0.372	-0.469	2.351	8.909
c_4	0.018	0.145	0.236	0.396
c_5	0.98	0.116	-0.394	2.926
c_6	0.0	0.748	1.615	-1.28
c_7	0.0	0.041	-0.044	0.037
c_8	1.0	0.221	-0.0537	-15.236
c_9	0.0	0.657	1.805	16.757
c_{10}	0.0	0.044	-0.037	-0.006

Rotational Torque: $C_R = r_1(Re_R)^{r_1} + \frac{r_3}{(Re_R)^{r_4}}$.

Coefficient	Ellipsoid (5/2)	Ellipsoid (5/4)	Disc	Cylinder
Symmetric: r_1	0.23	0.573	3.812	0.024
Symmetric: r_2	-0.116	-0.154	-0.13	0.168
Symmetric: r_3	96.378	116.61	283.03	77.314
Symmetric: r_4	1.0	1.0	1.0	1.0
Non-symmetric: r_1	71.03	1.244	13.31	239.76
Non-symmetric: r_2	0.069	0.239	0.189	0.075
Non-symmetric: r_3	773.04	378.12	783.05	2074.02
Non-symmetric: r_4	0.67	0.789	0.628	0.612

Correlations from [16] for full rotational particle trajectories.

For $Re_p \in [1.21 - 240]$

Drag:

$$C_D(\alpha) = C_{D,0} + \left(C_{D,\pi/2} - C_{D,0}\right) \sin^2 \alpha,$$

$$C_{D,0} = \frac{24}{Re_p}\left[K_0(w) + 0.15w^{-0.8}Re_p^{0.687} + \frac{(w-1)^{0.63}Re_p^{0.41}}{24}\right], \quad C_{D,\pi/2} = \frac{24}{Re_p}\left[K_{\frac{\pi}{2}}(w) + 0.15w^{-0.54}Re_p^{0.687} + \frac{w^{1.043}(w-1)^{-0.17}Re_p^{0.65}}{24}\right]$$

Lift:

$$C_L = \left[F_L(w) Re_p^{0.25} + \frac{G_L(w)}{Re_p^{0.755}} \right] \cos(\alpha) \sin^{1.002^{Re_p}}(\alpha),$$

$$F_L(w) = 0.1944(w^{-0.93} - 1)\ln(w) + 0.2127(w - 1)^{0.47}, \quad G_L(w) = 0.9183(w - 1)^{0.46}\ln(w) - 4.0573(w^{-1.61} - 1).$$

Pitching Torque:

$$C_T = \begin{cases} \ln(w)\left[\frac{F_T(w)}{Re_p^{0.18}} + \frac{G_T(w)}{Re_p^{0.51}}\right]\cos^{0.9994^{Re_p}}(\alpha)\sin(\alpha), F_T(w) = 6.46(w^{-0.2212} - 0.4855), G(w) = 0.072(w - 1)^{1.85}, w \in [1,10] \\ \left[\frac{F_T(w)}{Re_p^{0.3}} + \frac{G_T(w)}{Re_p^{0.9}}\right]\cos^{0.9989^{Re_p}}(\alpha)\sin(\alpha), F_T(w) = 1.67\ln(w)(w - 1)^{0.24}, G(w) = -2.71\ln(w) + 0.28\left((w^{1.65} - 1) + (w - 1)^{-0.22}\right), w \in [10 - 32] \end{cases},$$

Correlation from [21] for non-spherical drag law with sphericity

$$C_D = \frac{24}{Re\ K_1}\left(1 + 0.1118(Re\ K_1\ K_2)^{0.6567}\right) + \frac{0.4305 K_2}{1 + \frac{3305}{Re\ K_1 K_2}} \text{ for } Re\ K_1\ K_2 \leq 10^5.$$

$$K_1 = \left(\frac{1}{3} + \frac{2}{3}\phi^{-\frac{1}{2}}\right)^{-1} - 2.25\frac{d_p}{d_{tube}}, \text{ or } K_1 = \left(\frac{1}{3} + \frac{2}{3}\phi^{-\frac{1}{2}}\right)^{-1} \text{ if not settling in a tube.} \quad K_2 = 10^{1.8148(-\log_{10}\phi)^{0.5743}}$$

OpenFOAM spherical drag law:

$$C_D = 0.424\ Re, \qquad Re > 1000$$

$$C_D = 24\left(1 + \frac{1}{6}Re^{\frac{2}{3}}\right), \qquad Re \leq 1000$$